An elasto-plastic fracture mechanics based model for assessment of hydride embrittlement in zircaloy cladding tubes

Karl-Fredrik Nilsson *, Nikola Jakšić, Vratko Vokál

European Commission, DG-JRC, Institute for Energy, P.O. Box 2, 1755 ZG Petten, The Netherlands

ARTICLE INFO

ABSTRACT

This paper describes a finite element based fracture mechanics model to assess how hydrides affect the integrity of zircaloy cladding tubes. The hydrides are assumed to fracture at a low load whereas the propagation of the fractured hydrides in the matrix material and failure of the tube is controlled by non-linear fracture mechanics and plastic collapse of the ligaments between the hydrides. The paper quantifies the relative importance of hydride geometrical parameters such as size, orientation and location of individual hydrides and interaction between adjacent hydrides. The paper also presents analyses for some different and representative multi-hydride configurations. The model is adaptable to general and complex crack configurations and can therefore be used to assess realistic hydride configurations. The mechanism of cladding failure is by plastic collapse of ligaments between interacting fractured hydrides. The results show that the integrity can be drastically reduced when several radial hydrides form continuous patterns.

© 2009 Elsevier B.V. All rights reserved.

1. Introduction

Intermediate long-term storage of spent nuclear fuel is an integrated part of radioactive waste management strategies in many countries [1–3]. Storage times up to 50 years were considered in the past but much longer storage times, up to 300 years, are now also considered. Safety under normal, off-normal and accident conditions is ensured by the facility and the container where the spent fuel is placed. The fuel cladding constitutes the first barrier against release of radionuclides and its integrity is therefore crucial. In geological disposal on the other hand there is generally no credit for the cladding as a barrier. Spent fuel storage has an excellent safety record and claddings that have been in dry storage for a few decades are generally in good state [4,5], but the new trends with higher fuel burn-up (>65GWd/MTHm) and reprocessed fuels such as MOX fuel, which lead to higher temperatures and stresses, and the much longer storage times has lead to an increased need of further studies to ensure continued safety.

The fuel cladding in most of today's Light Water Reactors (LWR) is made of zirconium alloys such as Zircaloy-2 for Boiling Water Reactors (BWR) and Zircaloy-4 for Pressurized Water Reactors (PWR). For the integrity assessment all relevant degradation and failure mechanisms need to be considered [6,4]. In addition to irradiation damage the cladding corrodes during the reactor operation whereby an oxidation layer develops and hydrogen is picked up

[7]. When the spent fuel is removed from the reactor and put into wet storage the hydrogen precipitates as hydrides. The hydrides often appear in more concentrated form as a hydride rim close to the surface and as individual elongated hydrides aligned primarily in the circumferential direction due to the metallurgical texture of the tube [8]. The internal pressure at room temperature is typically 3–7 MPa [9]. When the spent fuel is transferred from wet to dry storage the temperature increases to 400 °C, the hydrides dissolve and the pressure increases (6–16 MPa). The hydrides are then re-recitated as partially radial hydrides as the temperature drops. This hydride re-orientation is a function of the temperature and the hoop stress. At 400 °C typical threshold values for re-orientation are 60–100 MPa [10,11]. The ratio between the radius and the wall thickness is typically 8 for cladding tubes so the hoop stress (pR/t) is sufficient for hydride re-orientation. It was shown in the early 1960s by Louthan and Marshall [12,13] that radial hydrides may drastically reduce the ductility of zircaloy claddings. There is also a large number of more recent data that demonstrate the ductility reduction under ring-compression, tensile and pressure tests [14–19]. The hydride effect may actually be stronger for a modest hydride content (100–200 ppm) than for a very high hydride content (1000 ppm). One explanation is that more long radial hydrides may be formed with the lower content [14,10], but the interaction between hydrides and percentage of re-dissolution will also play a role. It should be noted though that the strength may increase with increased hydride content, in particular for circumferential hydrides, and this effect is stronger for higher temperatures [20,18,21]. The increased strength is because hydrides are stiffer than the matrix and hence this increase of the strength applies

only to non-fractured hydrides. Radial hydrides, however, fracture at low loads and the strength is then also generally reduced, although much less that the total elongation [14,15].

Creep is the major failure mechanism considered under normal conditions. It has been demonstrated that creep rupture strain may be significantly reduced by radial hydrides [16,22,23]. Delayed hydride cracking (DHC), where dissolved hydrogen migrates towards existing small cracks and precipitates, is the second potential time dependent failure mechanism [24]. Most studies indicate that claddings should not fail by creep or DHC under long-term storage conditions due to the relatively low stresses and temperatures that also decrease with time. For creep a 1% strain criterion is often used and considered to give sufficient safety margin. For future long-term spent fuel storage with higher burn-up and increased radial hydride content this needs to be verified. There are however recent studies that indicate that DHC failure may occur after several decades of long-term storage [25]. In transport and for off-normal and accident conditions in long-term storage the cladding may be subjected to impact loads and the impact energy, which can be significantly reduced by hydrides [26], is then a more relevant measure of the ductility.

Between room temperature and 300 °C the hydrides are much more brittle than the zircaloy matrix and hydrides crack when the strain component normal to the hydride reaches typically 1% [27–29]. The hydride fracture strain is however not purely a material property. Its deformation is a result of the interaction between the hydride and the matrix so the failure strain depends on the hydride length and the stiffness of the matrix [28], and δ-hydrides are generally more brittle than γ-hydrides, [20]. For pressurized tubes with a dominating hoop stress, this implies that cracking of radial hydrides precedes failure of the tube. It is natural to treat fractured hydrides as cracks and assume that crack growth can be modelled by fracture mechanics. With this assumption the load at which the component fails depends on the size, location and orientation of the hydrides as well as the material's fracture toughness. The size of individual hydrides may vary from less than a μm to several hundreds of μm in extreme cases [30–32,14,33]. The hydride orientation is primarily related to the stress directions, whereas the size of the hydrides depends on the temperatures involved and the rates, where very slow cooling times promotes long radial hydrides [34,33]. The fracture toughness of the hydrides is very low, 5–10 N/m from nano-indentation tests [35], as compared to 10–100 kN/m for zircaloy fracture mechanics tests [36–40], and the threshold fracture toughness for delayed hydride cracking (250–1000 N/m [24]).

Ductility loss induced by radial hydrides has been modelled by fracture mechanics [41] for specific crack configurations that allow semi-analytical expressions for J and crack-tip stresses and strains. With the view to analyse more complex hydride configurations a more general model is developed and presented in this paper. The most basic assumption is that hydrides can be modelled as cracks. An elasto-plastic fracture mechanics finite element analysis is then used to assess how the ductility is affected by hydrides. The analysis in this paper includes single straight and kinked cracks with different crack length, orientation and locations; two interacting cracks with different distances between them and a case with representative multi-crack configuration with different orientations.

2. Single and double crack analysis

Onset of crack growth is expected to take place when the J-integral attains a critical value, which we refer to as 'J_{IC}'. A fracture toughness value, J_{IC}, is normally determined from a specimen with a fabricated macro-crack under pure Mode I loading. The crack initiation from such tests is physically not well defined since it is impossible to distinguish between crack blunting and stable tearing. J_{IC} is therefore taken from the J with 200 μm apparent crack extensions, which is much larger than the typical distance between hydrides. Due to the small dimensions the 'J_{IC}' corresponds to a much smaller crack growth than a 0.2 mm offset value. The computed J-integral depends on the applied load and the size, location, orientation and shape of the crack but it is also affected by interaction between neighbouring cracks. The commercial finite element code ABAQUS has been used for all the numerical analyses. The finite element model is a two-dimensional plane strain cracked tube segment with section angle 20° and with symmetry conditions imposed on the ends (Fig. 2). A plane strain model is reasonable and captures the main features as long as the hoop stress is the dominant stress direction. A complete 3D model would also drastically increase the computational effort and the complexity of the finite element model. The inner and outer radii are 4.4165 mm and 5.0305 mm respectively, which gives a wall thickness of 614 μm. The finite element mesh is generated automatically by auxiliary python scripts that allow user-defined mesh refinements to ensure numerical convergence of the results. The number of degrees of freedom and the computational times depend on the crack configuration. The Young's modulus, the Poisson's number and the true stress–strain curve are given in Table 1 and in Fig. 1. The constitutive data are typical for Zircaloy-4 cladding at room temperature and have been provided by AREVA Fig. 1. The applied load is always monotonically increasing. There could in principle be very small regions with local unloading from load redistribution but there was no distinction in the stress-curve for loading and unloading in the analysis.

2.1. Single straight crack

The single straight crack is the simplest case that allows us to assess some relevant characteristics such as size, orientation and location of cracked hydrides, which influence the failure load in a fracture mechanics approach. Fig. 2 depicts the geometry parameters that were used to characterize a single straight crack. As seen in Fig. 2 two crack tip mesh types were adopted: a circular focused mesh with three collapsed nodes at the crack tip and a rectangular mesh. The analysis also included numerical convergence analysis where R_c varied from 0.1 μm to 50 μm. The element size in the crack tip region was prescribed to be one eighth of this value. The parameter values for the six single crack analyses are summarized in Table 2.

Fig. 3a depicts the computed J-integral versus the applied load for a radial crack with length 150 μm located in the center of the tube and for an inner surface breaking crack respectively (Case 1). The result is for crack tip B, but the value was almost identical for the crack tip A for the internal crack. The very steep increase in the computed J occurs when the ligament between the crack tip

Table 1
Parameter values.

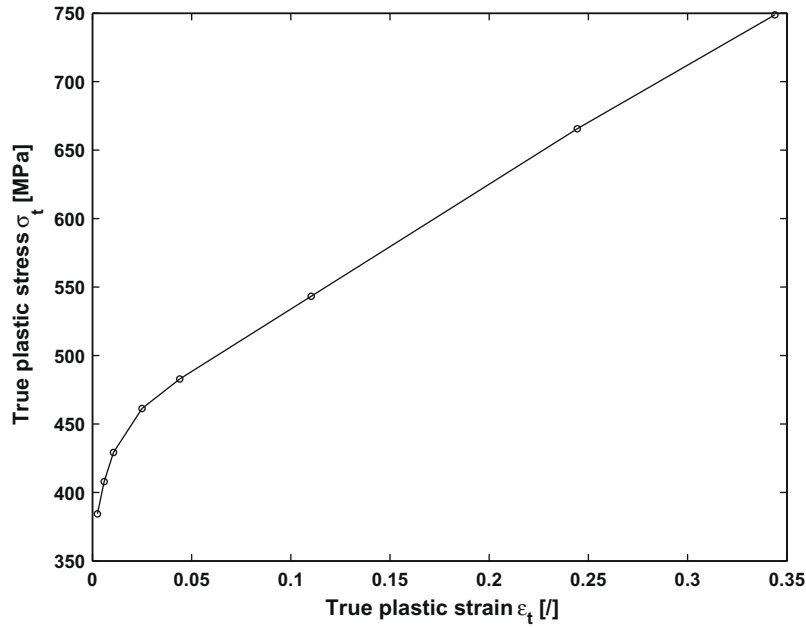| Parameter	Denotation	Value	Unit
Young modulus	E	100.5	GPa
Poisson number	v	0.3	–
True plastic stress and strain	$(\sigma_t, \varepsilon_t)$	(339.0, 0.0000)	(MPa, –)
		(384.4, 0.0025)	(MPa, –)
		(408.0, 0.0059)	(MPa, –)
		(429.3, 0.0106)	(MPa, –)
		(461.4, 0.0250)	(MPa, –)
		(483.0, 0.0440)	(MPa, –)
		(543.4, 0.1103)	(MPa, –)
		(665.8, 0.2444)	(MPa, –)
		(749.0, 0.3441)	(MPa, –)

Fig. 1. Experimental material data for the plastic region.
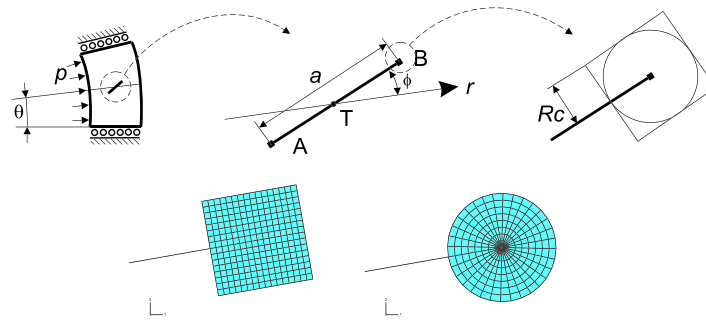

Fig. 2. Description of the geometrical parameters for the single crack model and the circular and square crack tip mesh configurations.

and the free surface is completely yielded. As expected J is systematically higher for the surface breaking defect. It can also be noted that J-values are low compared to the fracture toughness of zircaloys (10–100 kN/m with 0.2 mm off-set). The stiffness of the tube is also lowered by cracks. Fig. 3b shows the computed hoop strain ($\varepsilon_\phi = u_r/R$) at the inner surface versus the load. The steep increase in J and ε_ϕ coincides with plastic collapse of the tube.

As mentioned above this case was also used to assess the convergence and stability of the numerical results by varying the element size near the crack tip, comparing J for different contours and

comparing results from the circular and squared crack tip mesh. The computed J was insensitive to the crack tip mesh length when R_c was larger than 1 μm. Because the loading increases monotonically the J-integral should be independent of the contour from which it is evaluated. For the squared crack tip mesh there was no difference between J evaluated from different contours, whereas for the circular mesh the computed J was smaller for contours very close to the crack tip at onset of ligament yield. In the results presented for the rest of the paper a squared mesh with $R_c = 5$ μm has been used if not stated otherwise. This value is assumed to provide converged results. The single crack model with $R_c = 5$ μm had about 1.5×10^4 degrees of freedom.

The numerical results are affected by the boundary conditions. To assess this, the radial central crack analysis (Case 2) was performed with the crack located at different circumferential locations (θ in Fig. 2). A crack close to the symmetry line had a lower J and the 'end effect' increased with the applied load, but for $\theta > 3°$ it was negligible. In all cases below the cracks will be placed sufficiently far away from the symmetry boundary conditions to have negligible end effects.

The computed J-integrals versus crack length for a radial and centrally located crack (Case 3) are plotted in Fig. 4 for five pressure values ranging from 1.5 to 20 MPa. As mentioned above onset

Table 2
The crack parameter values for the single crack analysis, where T is center point with coordinates r and θ, ϕ is crack tilt angle, a is crack length, d is distance from crack tip A to the inner boundary and ψ is kink angle.

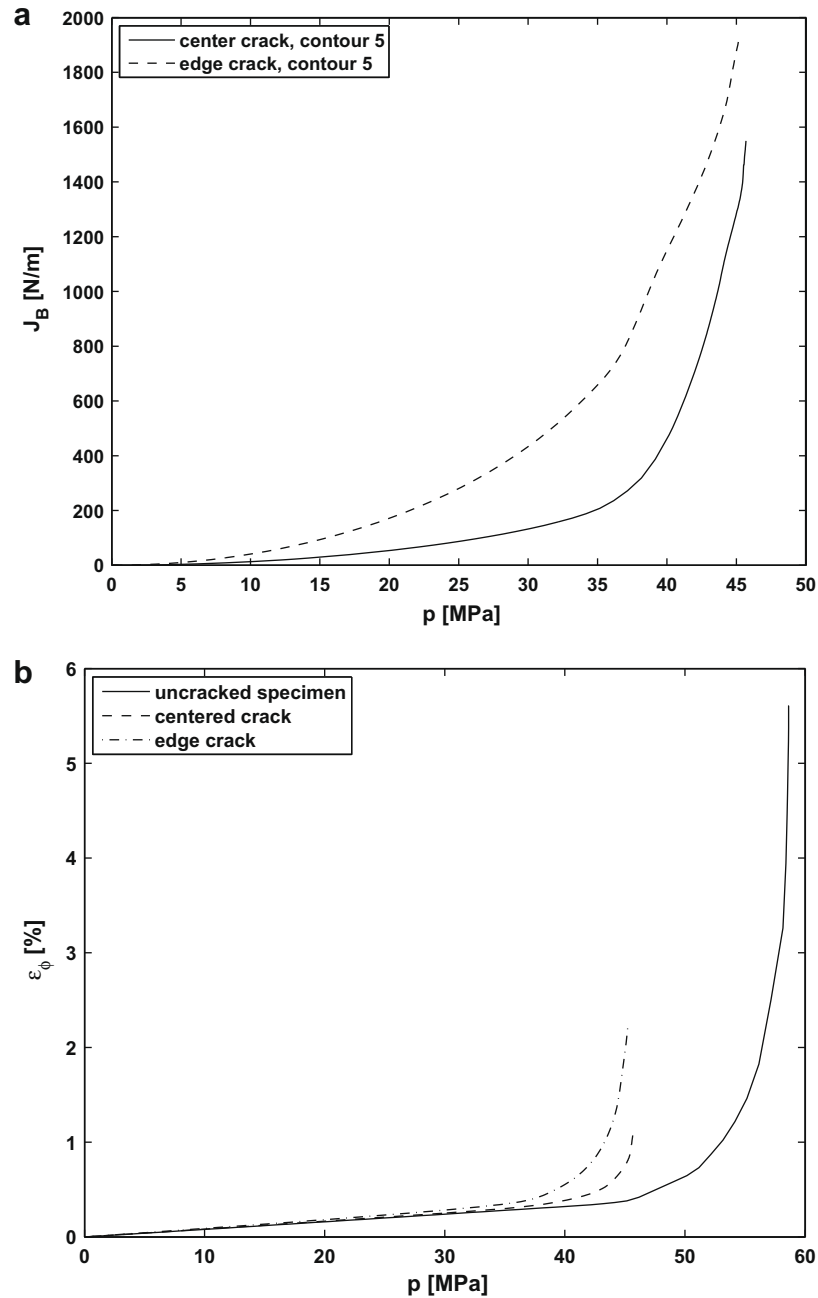| Case	$T(r;\theta)$(mm;°)	$\phi(°)$	a(μm)	d(μm)	$\psi(°)$
1	(4.7235; 10)	0	150	232 and 0	–
2	(4.7235; [0.2–5])	0	150	232	–
3	(4.7235; 10)	0	[10–550]	[32–302]	–
4	([4.9455–4.5015]; 10)	0	150	[10–454]	–
5	(4.7235; 10)	[0–180]	150	[232–307]	–
6	(4.7235; 10)	[−50 to 50]	150	[232–307]	[−30 to 30]

Fig. 3. (a) Computed J-integral versus applied load at crack tip B for a radial crack of length 150 μm that is located in the middle of the tube and at inner surface respectively (Case 1) and (b) the associated hoop strain ε_ϕ versus the load p for the uncracked specimen, single centered crack and single edge crack.

of crack growth can only be attained when the ligament yields and the J-values increases drastically. For a pressure of 7.5 MPa that requires a crack length of 500 μm.

The closer the crack is to the inner or outer surface, the lower the load will be when ligament yield occurs. This is illustrated in Fig. 5 (Case 4), where the computed J-integral for a radial 150 μm crack is plotted versus the distance to the inner surface for the same pressure levels as in Fig. 4.

Fig. 6 shows how the computed J-integral for a 150 μm crack located in the center of the tube is affected by the crack orientation at $p = 5$, 7.5, 10 and 20 MPa (Case 5). The computed J depends strongly on the crack orientation and it decreases monotonically as the crack rotates from the radial to the circumferential direction, and J is essentially zero when the crack is in the circumferential

direction. It can also be noted that the relative difference in the J-distribution increases with the load.

2.2. Single kinked crack

As a first approximation it is natural to assume cracked hydrides to be straight cracks as in the examples above. In reality the geometry is more complex. At a macro-level hydrides are often kinked and at a micro-level hydrides always contain a large number of small kinks. When the crack tip loading is mixed mode (Mode I opening and Mode II in-plane shearing), the crack will generally kink at onset of crack growth and the kink angle is determined from the condition that the crack tip loading is pure Mode I or maximum energy release rate [42]. A less restrictive
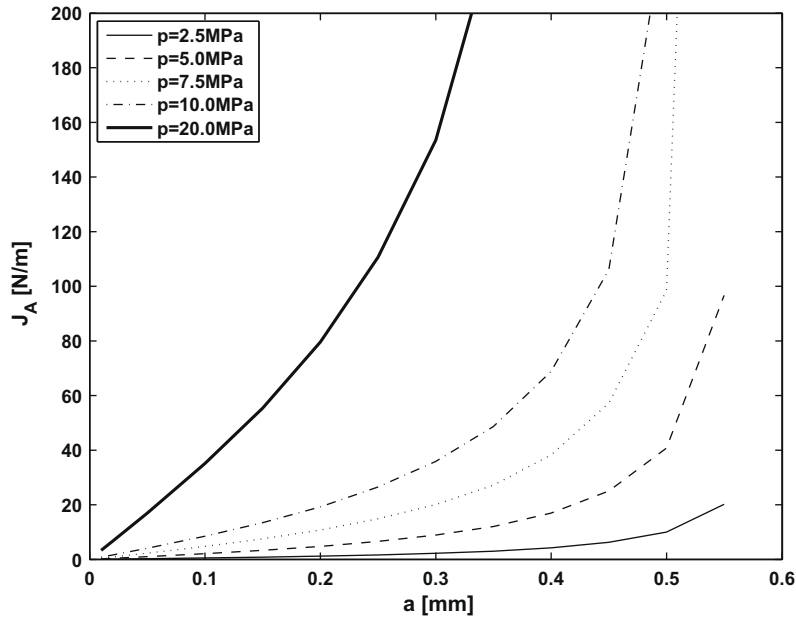
Fig. 4. Computed J-integral for crack tip A versus crack length for $p = 2.5, 5, 7.5, 10$ and 20 MPa.
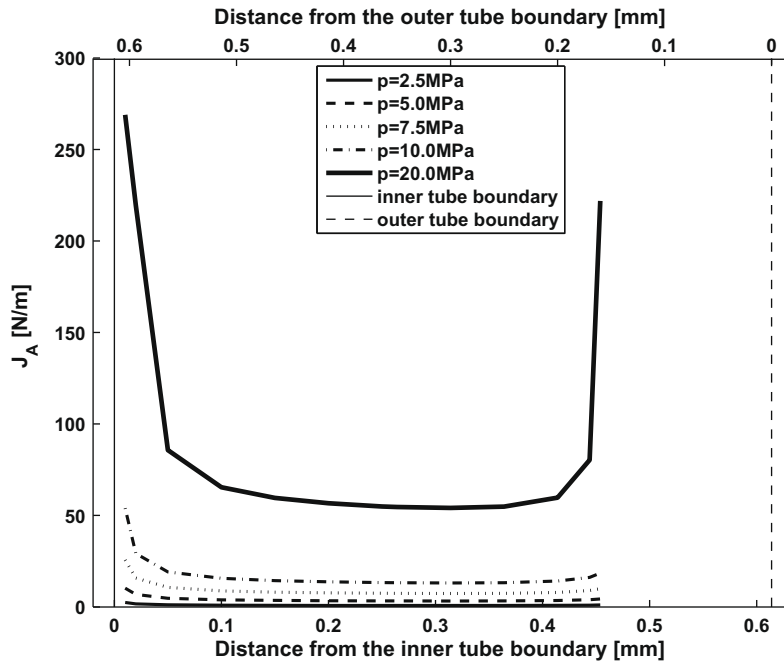

Fig. 5. Computed J-integral at crack tip A versus distance from the inner tube surface for $p = 2.5, 5, 7.5, 10$ and 20 MPa.

assumption is to model the fractured hydride as a kinked crack as in Fig. 7. To assess how a small kink affects the computed J, the fracture analysis was performed for a 150 μm crack rotated in the interval ±50° from the radial direction and where the crack was kinked by an interval $\psi = [-30°, 30°]$ from the radial direction with 5° increments and where the length of the kinked part was 1.5 μm.

Fig. 8 shows the computed J versus the crack orientation for a straight crack and a kinked crack respectively at $p = 10$ MPa. For the kinked crack the kink angle that maximizes the J is computed

using cubic spline interpolation. This angle is given in Table 3 for the different orientation angles. The important observation is that a small kink increases the computed J for non-radial cracks, which significantly flattens the J-distribution and cracks that are tilted in the interval ±50° from the radial direction are equally critical. The tilt angle in an elastic analysis increases with the mode mixity [42], which is in line with the results in this paper. For a radial crack the loading is pure Mode I and the shearing component (Mode II) increases as the crack becomes more circumferential. For practical reasons hydrides that are within ±45° from the radial direction

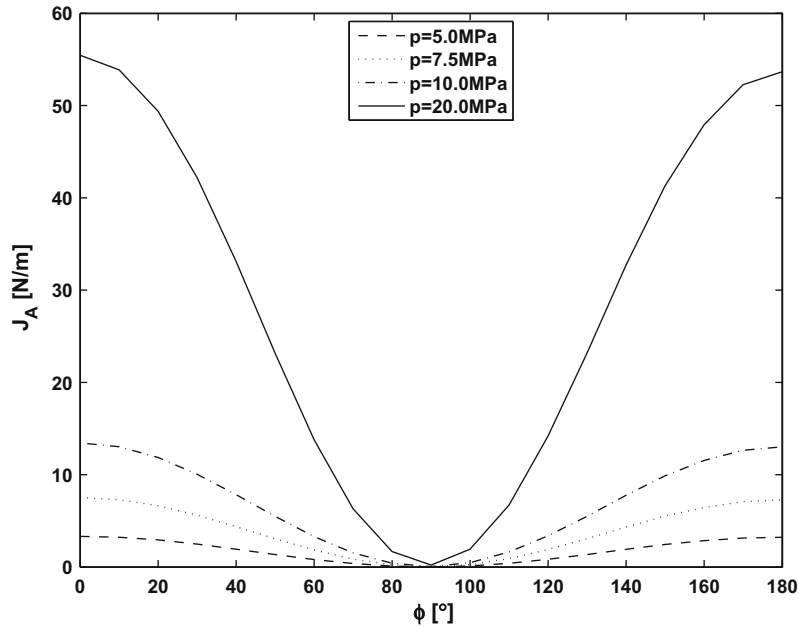**Fig. 6.** Computed *J*-integral at crack tip A versus crack orientation for *p* = 5, 7.5, 10 and 20 MPa.
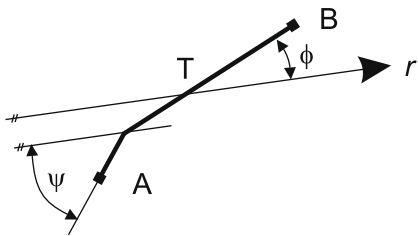

Fig. 7. The parameters used to describe the kinked crack.

are often defined as re-oriented. The results in Fig.8 indicate that such a characterization makes sense in a fracture mechanics approach. To model the small kink, the squared element size, R_c

was reduced to 0.3 μm. The number of degrees of freedom increased drastically to typically 3×10^5. It can be seen that the *J* value for the kinked (dotted line) and straight crack model (solid line) give the same result for a radial crack. Thus the difference in R_c did not affect the result. For each crack orientation 13 kink angles were evaluated and the total computational times were consequently much higher than for a straight crack analysis.

2.3. Two interacting cracks

A zircaloy cladding tube may contain a very large number of hydrides where the distance between hydrides is smaller that the length of individual hydrides. This indicates that cracked hydrides will interact in a complex manner that depends on the size, orientation and distance between adjacent hydrides.
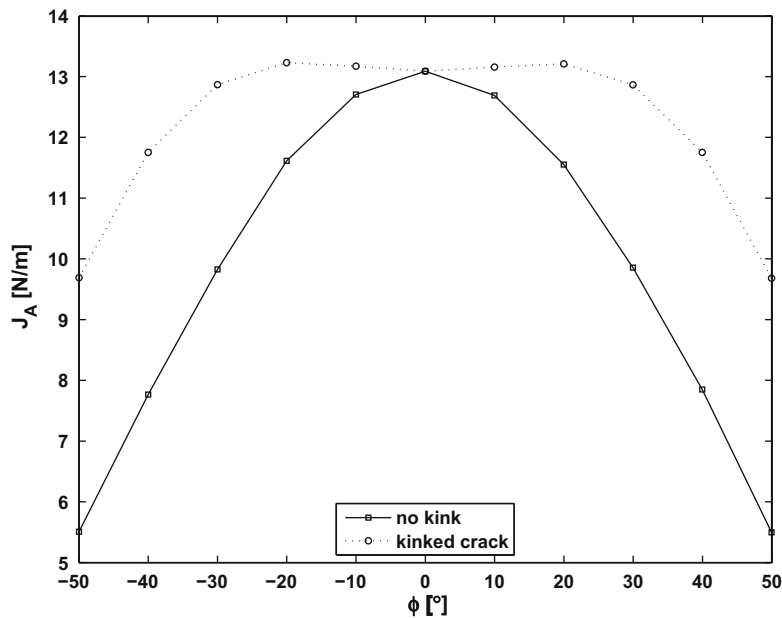

Fig. 8. Computed *J*-integral value at crack tip A for kinked crack □ and crack with no kink ○, *p* = 10 MPa.

Table 3
Single kinked crack's analysis results.

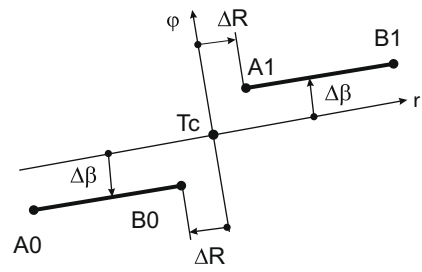| Crack rot.	No kink at crack	Kinked crack	
$\phi(°)$	J (N/m)	J (N/m)	$\psi[°]$
−50	5.508	9.693	11.2
−40	7.769	11.757	12.1
−30	9.831	12.874	11.7
−20	11.619	13.236	8.9
−10	12.713	13.178	4.5
0	13.095	13.096	−0.4
10	12.697	13.164	−4.7
20	11.557	13.218	−8.6
30	9.859	12.873	−12.6
40	7.852	11.757	−12.8
50	5.497	9.685	−10.7

Fig. 9. Geometry settings of the two crack model.

To assess such interaction the analysis was conducted for two equally sized radial 150 μm cracks where the distance between the crack tips was defined by ΔR and by the angle $\Delta\beta$ as defined in Fig. 9. ΔR and $\Delta\beta$ are measured from the central point $T = (4.7235\,\text{mm}, 10.0°)$. In the analysis ΔR was in the interval
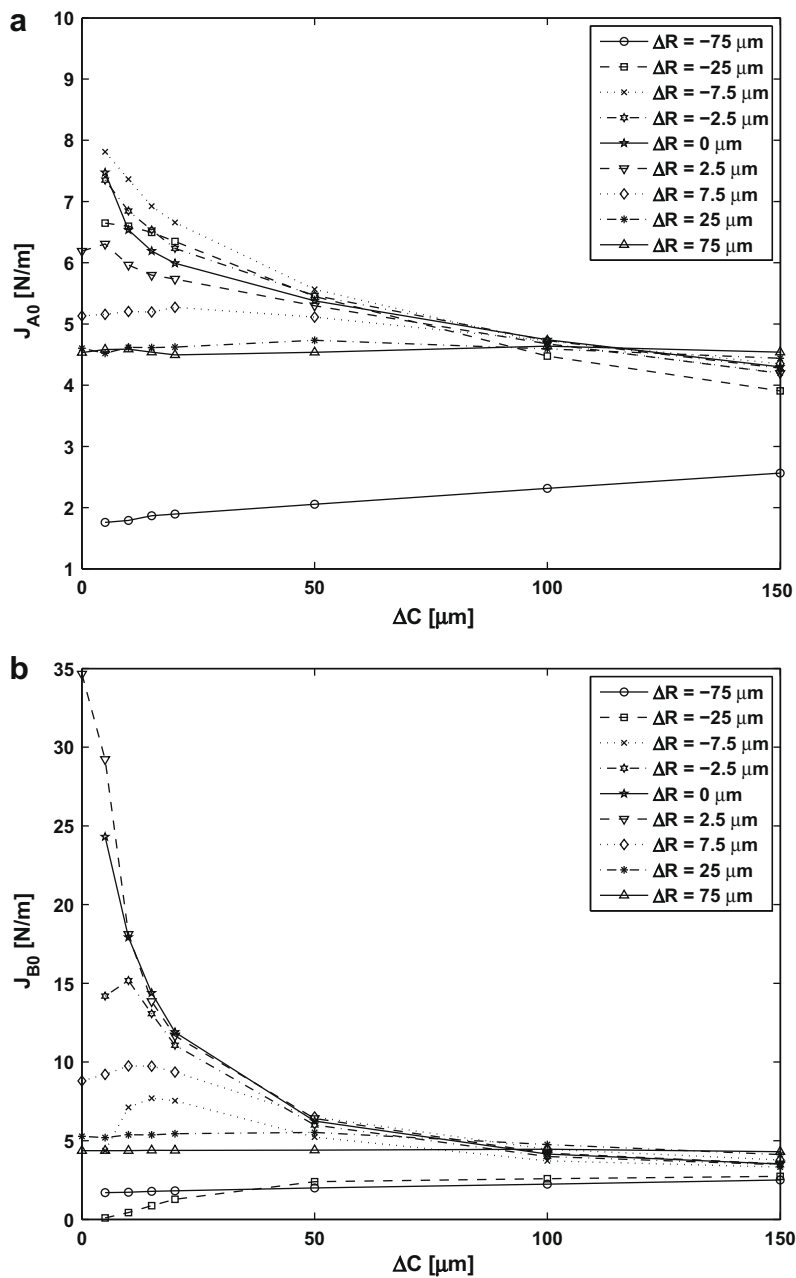

Fig. 10. Computed J-integral versus ΔC for crack tip A0 (a) B0 (b) at p = 5 MPa.

±57 μm and 2$\Delta\beta$ between 0° and 1.8195° (which corresponds to a circumferential distance, $\Delta C = 2\Delta\beta \cdot \pi R_{T_c}/180 = 150$ μm). A negative ΔR implies overlapping of cracks. The analyses were performed for a load up to 20 MPa.

The computed J at $p = 5$ MPa for the crack tips A0 and B0 versus ΔC are plotted in Fig. 10a and b respectively for different values of ΔR. Fig. 11a and b show the corresponding J-values versus ΔR for different ΔC. It follows directly that there is a strong crack interaction effect when the cracks are close to each other. For a positive ΔR, the interaction factor increases monotonically with decreasing distance and for negative ΔR there is a shielding effect if the overlap is large due to local unloading. When the overlap is very small the interaction becomes very complex. The J-integral value increases when ligaments yield and consequently the crack interaction is expected to extend to larger crack distances with increasing yielding. One therefore expects the crack interaction to be more

pronounced with increasing load. This is illustrated by Fig. 12 where the computed J is plotted for crack tip B0 for $p = 5$, 10 and 20 MPa and $\Delta C = 5$ μm.

3. Multi crack configuration

In this section we will analyse a more realistic crack configuration. To this end we use a set of 24 hydrides located primarily in the circumferential orientation. The micrographs were taken directly from [11] and analysed by an in-house image processing tool that uses the MATLAB image processing tool box. Fig. 13a shows the micrograph picture after it has been digitalized into a numeric matrix and contrasted by image processing procedures so that the darker hydrides appear more clearly. Each hydride was subsequently characterized with respect to its length (a), location $T(r; \theta)$ and orientation (ϕ). The mapped hydrides are represented
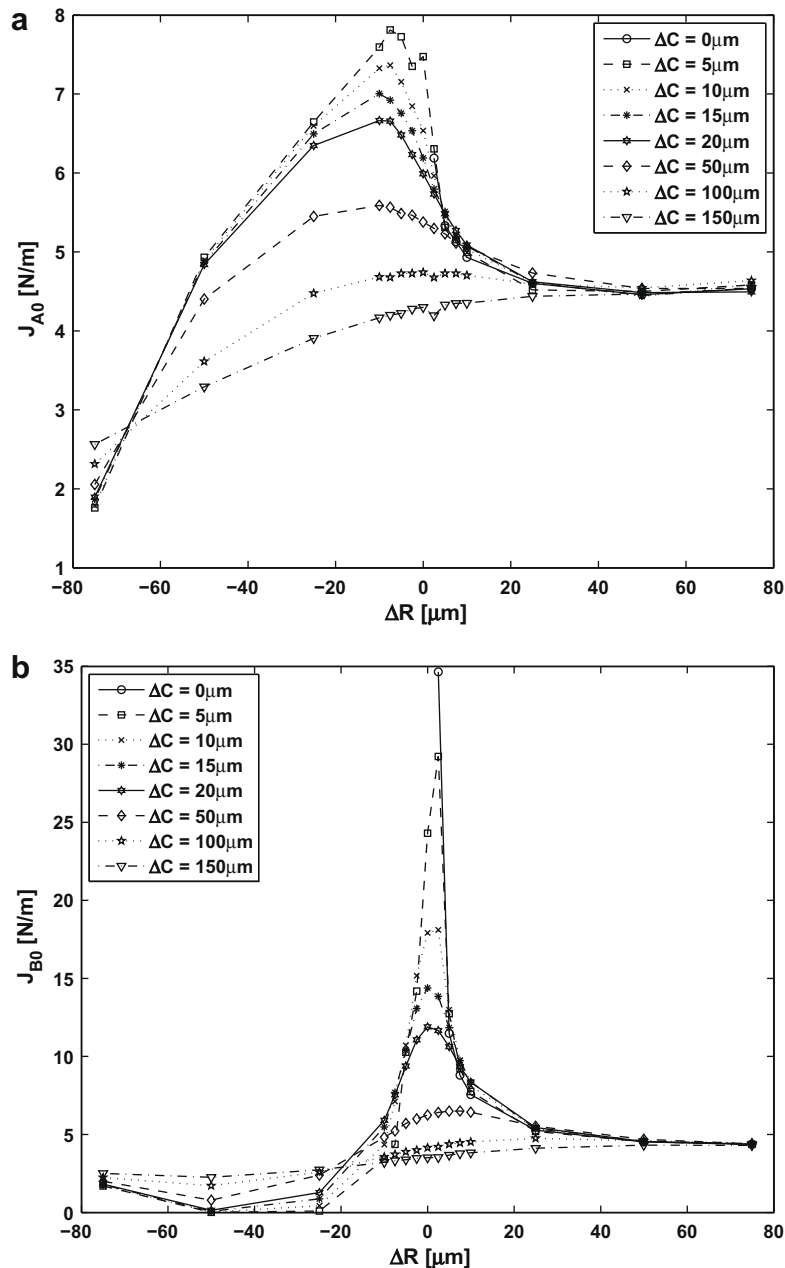

Fig. 11. Computed J-integral versus ΔR for crack tip A0 (a) and B0 (b) at $p = 5$ MPa.
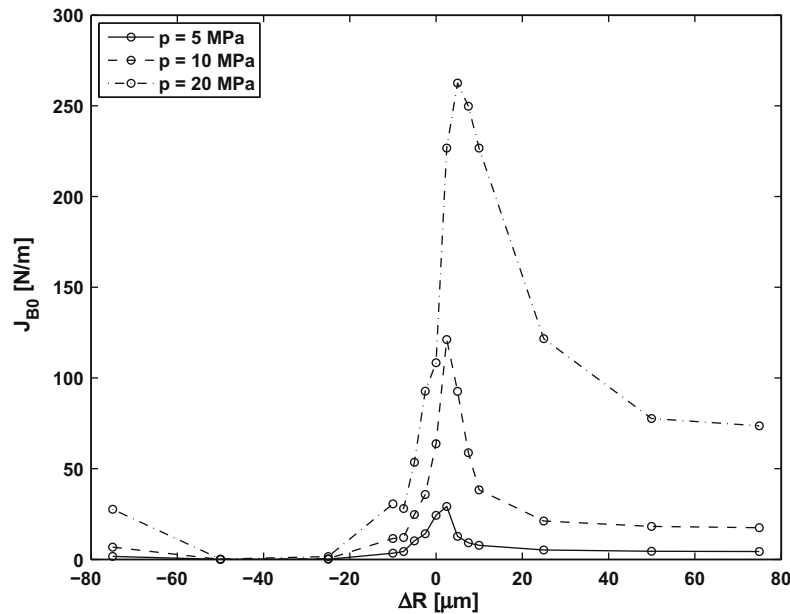
Fig. 12. Computed J-integral versus ΔR: crack tip B0 for $\Delta C = 5\ \mu m$ and $p = 5$, 10 and 20 MPa.

as yellow lines in Fig. 13b and the crack pattern with individual crack indices are shown in Fig. 13c.

The only simplification up to this stage is that each hydride is a straight line. The maximum, median and standard deviation of the hydride length was 169, 42 and 39 μm. It can also be seen that the typical distance between hydrides is 10–20 μm. A similar median and standard deviation values as in Fig. 13a can be found in [11] for a case taken after 10 thermo-mechanical load cycles with 48 hydrides that had undergone partial re-orientation and where the maximum length was 257 μm.

The final step is to create the finite element mesh for the particular crack configuration using the automatic python scripts with the requirement that each crack tip is modelled by the squared crack tip mesh and with $R_c = 5\ \mu m$ as the default value. The meshing becomes very complex and the mesh density may become extremely fine for specific crack configurations, in particular when there are small cracks very close to other cracks. This may also lead to numerical convergence problems due to locally very deformed meshes. To alleviate this problem the crack configuration from the image processing was slightly adjusted. Fig. 13d shows the resulting crack configuration used in the finite element model. The cracked area was about 400 μm × 400 μm and located centrally between the outer boundaries of the pipe segment. The number of degrees of freedom for the model is around 1.5×10^6. The finite element mesh is not shown since it is very fine and the segment would appear completely black.

To analyse the re-orientation, this crack configuration was rotated from the circumferential direction ($\vartheta = 90°$) to the radial direction ($\vartheta = 0°$) with increments of $-22.5°$. The corresponding crack configurations are shown in Table 4 as Cases 1–5. As shown in the single crack case, the J-integral increases if a crack is close to a free surface. A Case 5 was therefore defined by translating the radial crack configuration towards the inner surface of the pipe. The J-integral values are controlled by the yielding of the material in the cracked configuration and the failure load will be reduced if the uncracked part gets smaller. A sixth case (Case 6) was generated from Case 5 by taking one part of the crack configuration and distribute it at the outer surface to have cracks across the entire wall thickness. The finite element analysis did not include contact and crack surfaces could in prin-

ciple overlap. Contact and crack closure could be expected for cracks in the circumferential direction. To check that this did not affect the computed J for the dominant cracks we also performed an iterative set of analyses for Case 1 where overlapping cracks were removed and the model re-analysed. In the final state only three cracks remained open. All the J-values reported are for open cracks.

In Fig. 14 the computed maximum J-integral is plotted as function of the applied load for the seven different cases. The fourth, fifth and sixth column in Table 4 give the maximum load, the number of cracks with crack surface overlap (closed cracks) and the crack index with the peak J-integral values. The maximum load is the computed load at which numerical convergence problems occurred. The convergence problems are linked to a distorted finite element mesh at a crack tip, which would coincide with ligament yield and steep increase in the computed J. More than one crack index indicates that the crack tip with the maximum J-value changed as the load increases. Fig. 15 shows the computed J-integral for each of the 24 cracks for Cases 5 and 3 respectively at $p = 25$ MPa. From this analysis one can conclude that the failure load is strongly affected by the crack orientation, their location and by the extension of the cracked region. The load at which the J has a strong gradient for Case 1 in Fig. 14 is almost the same as the load at which the radial strain also had a strong gradient for the uncracked tube in Fig. 3b; both are governed by plastic collapse of the tube.

Fig. 16 shows the von Mises effective stress contours for Case 7 at $p = 10$ MPa and $p = 14.4$ MPa. The yellow, red and gray areas correspond to yielded material. The stress contours clearly illustrate the yielding of ligaments between the large cracks; at $p = 10$ MPa the ligaments have just yielded whereas at $p = 14.4$ MPa the ligaments are well into the yielded region and with several percent of strain. It can also be noted that the plastic zone between the ligaments is very localized and narrow in shape as opposed to the plastic zone between the crack and the free surface.

The example here, where hydrides are rotated as geometrical entities, is of course artificial. For hydride re-orientation to take place, the hydrogen needs first to be dissolved and then migrate by diffusion and re-precipitate as hydrides with an orientation that
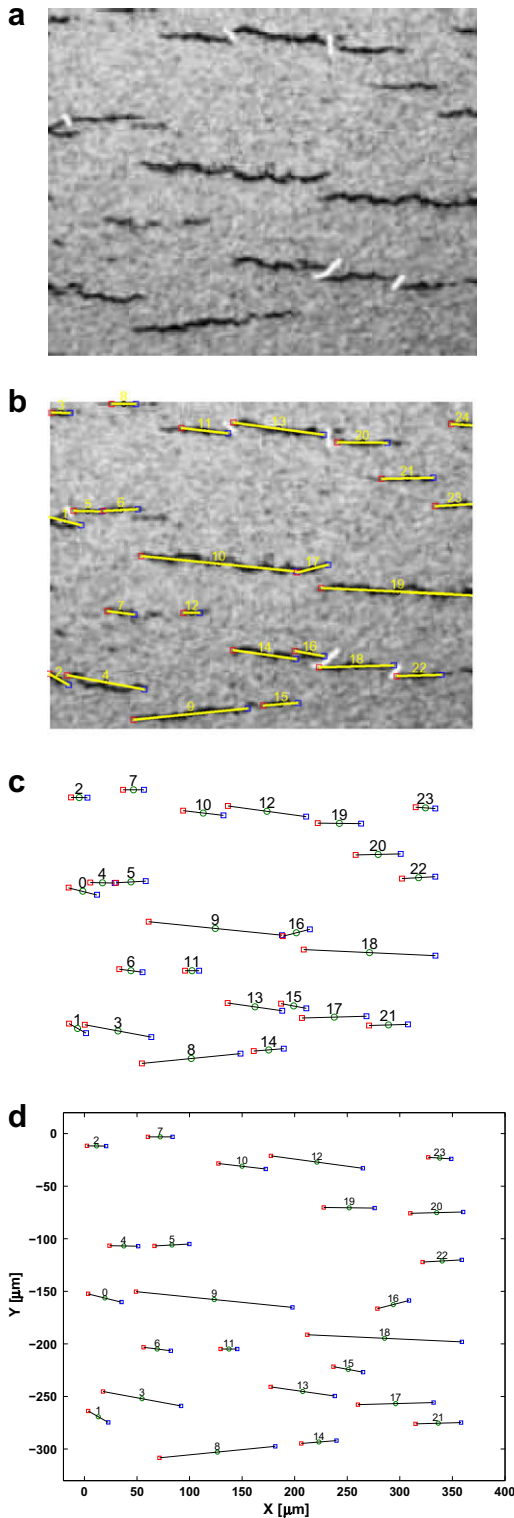
Table 4
Pattern rotation cases overview.

Case	γ (°)[a]	Picture	p_m (MPa)[b]	$N°$[c]	C-CT[d]
1	90.0		55.0	18	1B
2	67.5		40.8	6	9A → 9B → 9A
3	45.0		32.6	1	9A → 9B
4	22.5		29.5	1	9B → 18A
5	0.0		28.0	0	9B → 9A
6	0.0,nb		22.7	0	9B → 9A → 0B
7	0.0,ww		14.4	0	18A → 9B → 9A

nb = Near boundary, ww = whole width.
[a] Rotation angle.
[b] Load at which the numerical divergence has occurred.
[c] Number of the closed cracks.
[d] A crack index and a crack tip where the maximal value of the J-integral is reached.

Fig. 13. Schematic illustration of the steps to define the crack real configuration in a finite element model (a) micrograph with hydrides (b) hydrides marked from image processing (c) hydrides with indices after image processing (d) cracks with indices as used in the finite element.

4. Analysis of co-linear crack configurations

The hydrides in a zircaloy cladding tube have a very complex pattern and it is impossible from a practical point-of-view to assess every combination. The number of hydrides, their length, the ligament lengths and the circumferential distance are important crack characteristics. For a more systematic analysis a set of 12 co-linear radial crack configurations described by crack length (a), the number of cracks ($N°$), the normalized fracture area ($\xi_k = \sum_{i=1}^{N°} (a_k)_i/t$), where t is the tube thickness, k is the case index, and the angle between the cracks ($2\Delta\beta$) was defined. The mean circumferential distance is given by $\Delta C = 2\Delta\beta \cdot \pi R_{T_c}/180$. Table 5 gives the parameter configuration for each case together with a small picture of each crack configuration.

The computed J-integral versus the applied load are shown in Figs. 17–19. The maximum load and the crack tip with the highest J-value are given in Table 5. The crack indexing starts from the crack closest to the inner surface and the crack tip convention is the same as in Fig. 7.

Fig. 17 allows us to compare the effect of crack length, a, and the crack/ligament ratio, ξ. It is obvious that the failure load is much more affected by the crack/ligament ratio than the crack size. This is in line with the conjecture that failure is primarily controlled by ligament yield. As a consequence of the very non-linear stress–strain curve, the reduction in failure load is much stronger than

depends on the stress and texture. In [11] only relatively few hydrides were radial even after 10 thermo-mechanical load cycles. There are, however, many examples in the literature where most hydrides are radial after load cycles [14,10,15,30,22], so the Cases 5–7 are not unrealistic.
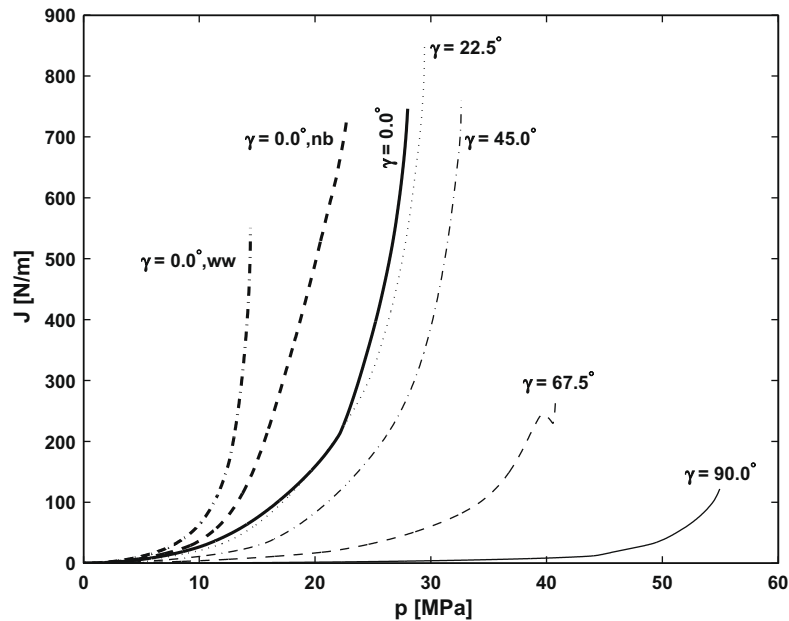
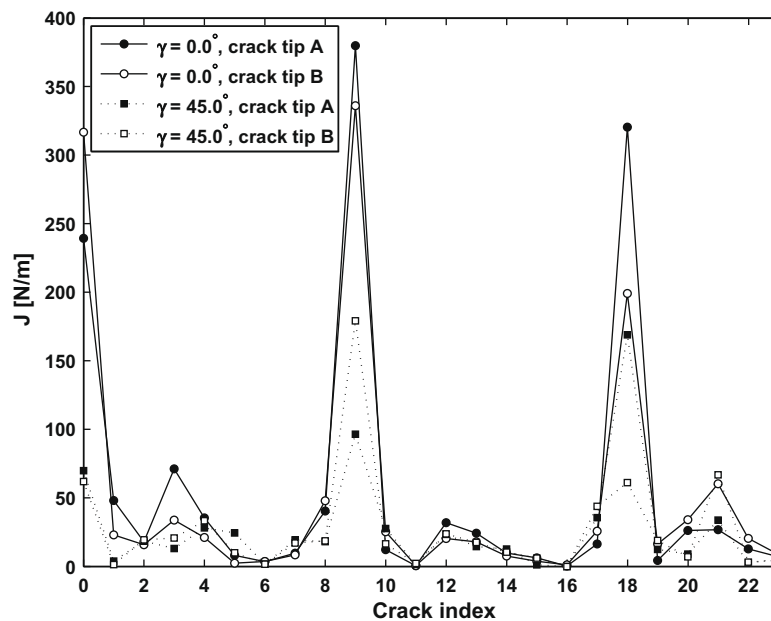**Fig. 14.** Computed maximal J versus the applied load for the different cases in Table 4.

Fig. 15. Computed J-integral values for $p = 25$ MPa for each crack for Case 4 ($\gamma = 0°$) and Case 2 ($\gamma = 45°$).

the reduction in the crack/ligament ratio. The computed J versus the load for the three different values of circumferential distance between the co-linear cracks is shown in Figs. 18 and 19 for crack lengths of 50 and 100 μm respectively. The load distribution is quite different when the cracks are spread out whereby the crack interaction becomes much weaker. This effect is more pronounced for the shorter crack since the ratio $a/\Delta C$ is twice as large. It also follows from Figs. 17–19 that the crack length has a relatively stronger effect when cracks are separated by a circumferential distance.

5. Discussion

In this paper we have assumed that hydrides first crack and that component failure can be modelled by classical fracture mechanics. Such an approach is by no means obvious since the geometrical scale of hydrides is quite small and the material is heterogeneous. One important question is which criterion one should use for the crack growth. It can be assumed that the crack growth occurs by successive tearing of ligaments between fractured hydrides as shown in for instance [8,31], but the concept of J-controlled fracture implies that J completely characterizes the crack tip situation. When the plastic zone is large compared to a characteristic length, such as the crack ligament, and the shape of the plastic zone depends on the crack geometry then one should not expect that a simple 1-parameter such as J is an accurate parameter for fracture. This is clearly the case here where the plastic deformation is constrained to the crack ligaments and therefore depends on the crack configuration. Another issue is the transferability of toughness data from large component tests. As mentioned above, a fracture toughness value, J_{IC}, is determined from a specimen with a fabricated
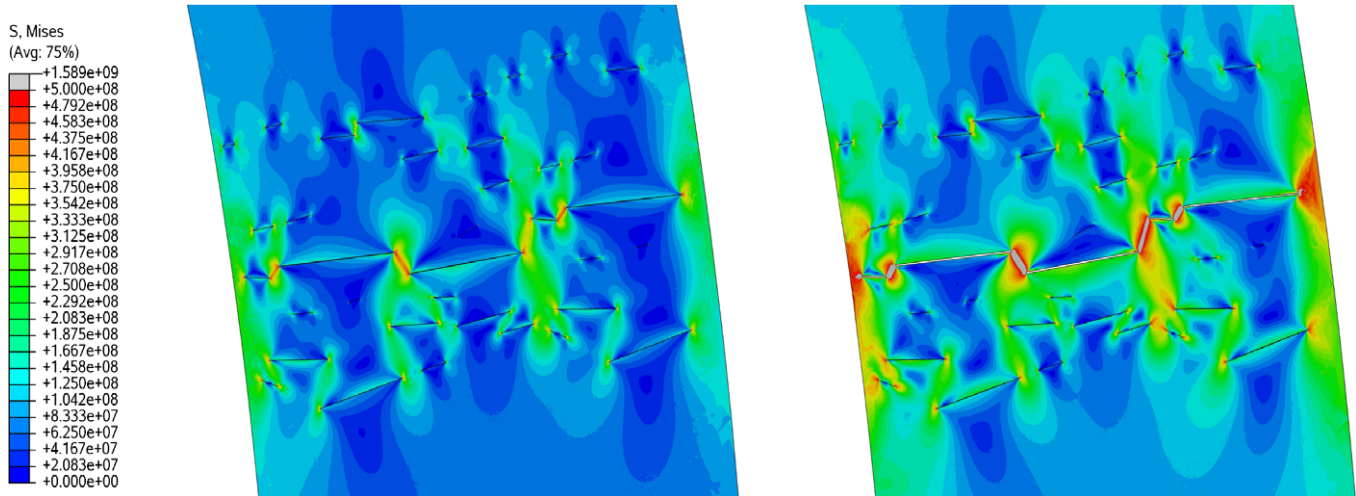
S, Mises
(Avg: 75%)
+1.589e+09
+5.000e+08
+4.792e+08
+4.583e+08
+4.375e+08
+4.167e+08
+3.958e+08
+3.750e+08
+3.542e+08
+3.333e+08
+3.125e+08
+2.917e+08
+2.708e+08
+2.500e+08
+2.292e+08
+2.083e+08
+1.875e+08
+1.667e+08
+1.458e+08
+1.250e+08
+1.042e+08
+8.333e+07
+6.250e+07
+4.167e+07
+2.083e+07
+0.000e+00

Fig. 16. Mises stress at $p = 10$ MPa and $p = 14.4$ MPa for Case 7.

Table 5
Different cases of the ligament analysis setting.

k[a]	a_k (μm)[b]	$N°$[c]	ξ_k[d]	$2\Delta\beta$ (°)[e]	Picture	p_m (MPa)[f]	C-CT[g]
1	50	10	0.814	0.0		14.1	$0B \mapsto 1A \mapsto 1B \mapsto 2A \mapsto 1B$
2	100	5	0.814	0.0		13.2	$0B \mapsto 1A$
3	50	8	0.651	0.0		24.9	$0B \mapsto 1A \mapsto 1B$
4	100	4	0.651	0.0		23.2	$0B \mapsto 1A$
5	50	6	0.489	0.0		34.7	$0B \mapsto 1A$
6	100	3	0.489	0.0		32.6	$0B \mapsto 1A$
7	50	10	0.814	0.1		15.0	$1A \mapsto 1B$
8	100	5	0.814	0.1		13.3	$0B \mapsto 1A$
9	50	10	0.814	0.3		21.7	$1A \mapsto 0A$
10	100	5	0.814	0.3		15.3	$0B \mapsto 1A \mapsto 1B \mapsto 0A$
11	50	10	0.814	0.6		33.7	$0A$
12	100	5	0.814	0.6		20.0	$0A$

[a] Case.
[b] Length of a crack.
[c] Number of cracks.
[d] $\xi_k = \sum_{i=1}^{N°}(a_k)_i/t$, portion of the tube wall cross-section occupied by the cracks.
[e] Circumferential distance between cracks.
[f] Load at which the numerical divergence has occurred.
[g] A crack index and a crack tip where the maximal value of the J-integral is reached.

macro-crack with 200 μm apparent crack extensions, which is much larger than the typical distance between hydrides. The localized plastic yielding of the ligaments as illustrated in Fig. 16 suggests that a cohesive zone with a crack tip opening displacement criterion could be a more appropriate model. On the other hand if the failure is controlled by ligament yield and plastic collapse, then fracture parameters (J, CTOD) will increase drastically and the load will be rather insensitive to the criterion for onset of crack growth. Hence J becomes a paremater for ligament yield. Zirco-

nium alloys usally exhibit crack growth resistance, i.e. the J-value needed to propagate the crack increases with the crack extension (R-curve) and build-up of a plastic wake behind the advancing crack tip. In a situation where crack propagation occurs by successive tearing of ligaments and crack coalescence, there would be no significant crack growth resistance since there was no tearing for the already cracked section. Moreover as the crack propagates the J-integral will also increase with the crack length. These two factors indicate an unstable crack growth mechanism. Although
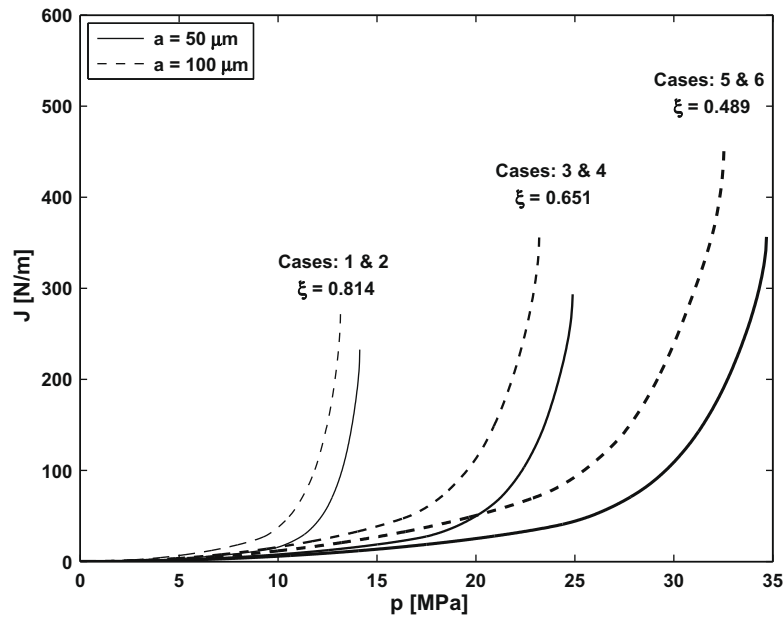
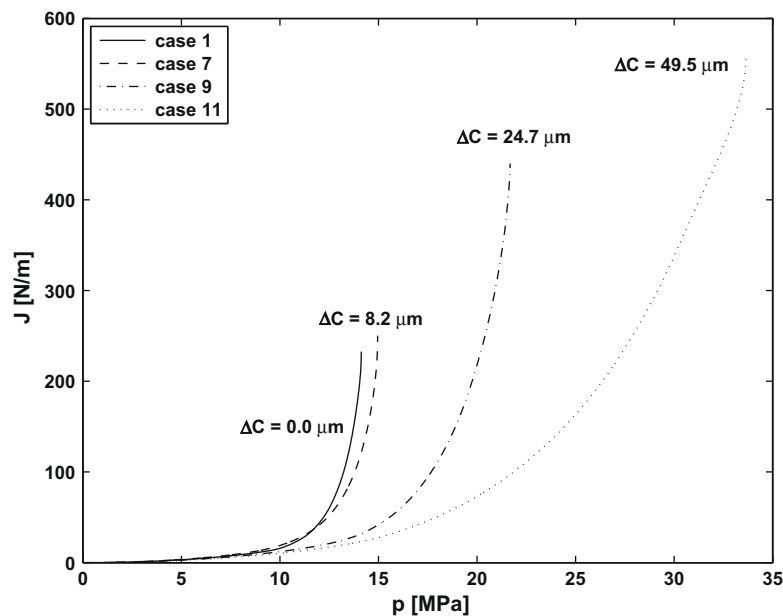**Fig. 17.** Computed *J*-integral versus applied load values for the Cases 1–6.

Fig. 18. Computed *J*-integral versus applied load values when a = 50 μm, $N° = 10$, $\xi = 0.814$ and $\Delta C = 0, 8.2, 24.7$ and 49.5 μm.

the propagarion is driven by the successive yielding of the ligaments and hence ductile, the global response may appear as more brittle since the load may be significantly lower than the global plastic collapse load. After re-orientation there will normally also be circumferential hydrides. Such hydrides could act as crack arresters either as 'crack branchers', if the hydride is fratured, or as inclusions if the hydride is intact and where the stiffness depends on the Zr/H ratio.

To verify the fracture model and to address fundamental issues we have started an experimental programme. In the test programme, hydrogen charged specimens with nominally 0, 100, 200 and 300 ppm of hydrogen will be tested. To create different hydride configurations, the specimens will first be subjected to thermo-mechanical load cycles with prescribed pressure at different temperatures. The specimens will subsequently be analysed by the image processing approach to quantify hydride configurations. The tested tubes will then be cut into smaller segments and loaded in radial displacement controlled tests until failure. The tests will be analysed using the model outlined in this paper.

In practice one does not know the hydride configuration. It depends on the stress and temperature history as well as the manufacturing process of the tube material. The first step in a total assessment would be to compute hydride uptake and nucleation, growth and precipitation from corrosion theories, hydrogen diffu-
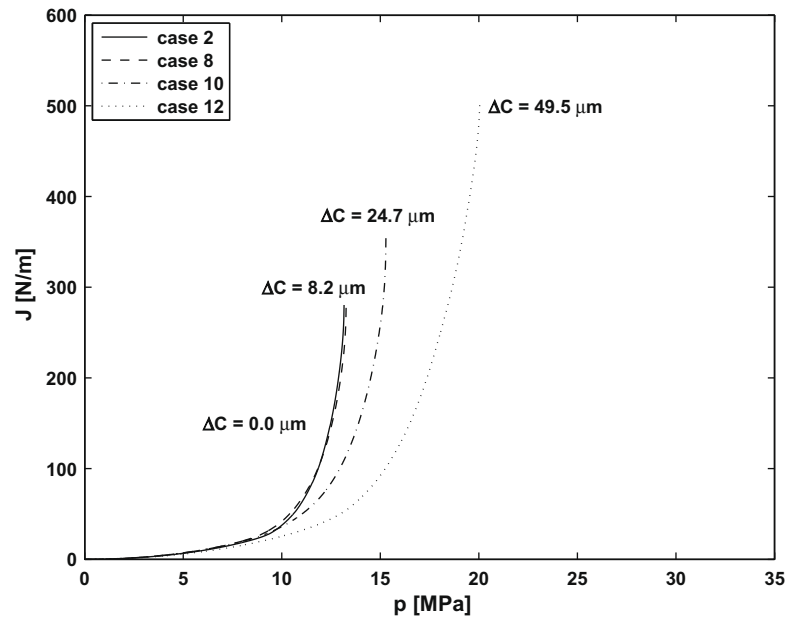
Fig. 19. Computed *J*-integral versus applied load values when *a* = 100 μm, *N*° = 5, *ξ* = 0.814 and Δ*C* = 0, 8.2, 24.7 and 49.5 μm.

sion and re-precipitation [33]. The second step is the fracture of the brittle hydrides that could probably be estimated by strain or stress criteria [20,43]. The final step would be the mechanical failure analysis studied in this paper. The complexity of the hydride configuration leads naturally to a probabilistic approach where failure is assumed to be governed by onset of crack growth. The *J*-integral needs to be computed for a set of given crack configurations, $J(p; a_i(T, \phi))$, and where cracks need to be described by some distribution function. Such an approach has been used to study how the ductility of ductile cast iron is affected by casting defects [44].

Hydride embrittlement is a key degradation mechanisms but there are others that affect the ductility of spent fuel claddings. Residual stresses result from the corrosion during operation and tensile stresses could be as large as 600 MPa at the outer surface [7]. Incorporating residual stresses in a finite element analyses can be rather straightforward since the value can be estimated from the volume difference between corroded and un-corroded material. The stress from the internal pressure will drop as the temperature drops unless additional gas pressure is built-up. One mechanism for increased gas pressure could be radioactive decay of alpha emitters which potentially could result in additional pressure of 12 MPa after 300 years of storage for MOX fuel [23]. The irradiation induces point and line defects that embrittle the material. To address this properly requires a multi-scale approach which is presently basic research and beyond engineering approaches. The approach for engineering analysis could be semi-empirical by determining the material properties such as fracture toughness and stress–strain curves experimentally and then using these data directly in the analysis.

6. Conclusions

The basic assumption in this paper is that hydrides are brittle and fracture at incipient global plastic deformation and that crack growth of fractured hydrides can be modelled with non-linear fracture mechanics. The hydride induced failure in cladding tubes for long-term storage is controlled by the hydride configuration and in particular the size, orientation of individual hydrides and the number of hydrides that interact in a complex way. The main conclusions from the analysis in these paper are:

- The load at which a cladding tube fails can be reduced by an order of magnitude and cladding failure become more unstable, as seen in Fig. 14, if there are several interacting radial hydrides across the wall thickness. The failure probability in a specific scenario would then be controlled by the probability of having a critical, but perhaps very local, hydride configuration.
- Hydride induced failure of zircaloy cladding is controlled by yielding of the ligaments between fractured hydrides as shown in Fig. 16. The relative length of hydrides across the wall thickness is therefore the parameter that most affects the failure load (Fig. 17).
- The probability for onset of crack growth from hydrides increases when hydrides become more radial as shown in Fig. 6.
- The distance between hydrides is often smaller than the length of the individual hydrides and crack interaction plays therefore an important role and must be accounted for.
- Hydrides have a complex shape and crack growth from non-radial cracks is more likely from kinked cracks (Fig. 8).

An experimental programme where the hydride configuration has been quantified, is needed to verify how well a fracture mechanics based model can predict failure loads. Such work has now started.

References

[1] The Roles of Storage in the Management of Long-lived Radioactive Waste – Practices and Potentialities in OECD Countries, 2006 NEA No. 6043.
[2] The Long-term Storage of Radioactive Waste: Safety and Sustainability – A Position Paper of International Experts, 2003 IAEA.
[3] Spent fuel performance assessment and research, Final report of a co-ordinated Research Project on Spent Fuel Performance Assessment and Research (SPAR) 1997-2001, 2003 IAEA-TECDOC-1343.
[4] Technical Basis for Extended Storage of Spent Nuclear Fuel, EPRI, Palo Alto, CA, USA, 2002 EPRI-Report-1003416.
[5] A. Sasahara, T. Matsamura, Nuclear Engineering and Design 238 (2008) 1250.
[6] Standard Guide for Evaluation of Materials Used in Extended Service of Interim Spent Nuclear Fuel Dry Storage Systems, 2004 ASTM Standard C1562-03.

[7] H.M. Chung, Hydride-related Degradation of SNF Cladding under Repository Conditions, Office of Civilian Radioactive Waste Management, ANL-EBS-MD-000011 REV 00 ICN 01, 2000.
[8] R.S. Daum, S. Majumdar, D.W. Bates, A.T. Motta, D.A. Koss, M.C. Billone, ASTM Special Technical Publication 1423 (2002) 696.
[9] R.E. Einziger, R. Kohli, Nuclear Technology 67 (1984) 107.
[10] H.C. Chu, S.K. Wu, R.C. Kuo, Journal of Nuclear Materials 373 (2008) 319.
[11] K. Sakamoto, M. Nakatsuka, Journal of Nuclear Science and Technology 43 (9) (2006) 1136.
[12] M.R. Louthan, R.P. Marshall, Journal of Nuclear Materials 9 (2) (1963) 170.
[13] R.P. Marshall, M.R. Louthan, ASM Transactions Quarterly 56 (1963) 693.
[14] H.C. Chu, S.K. Wu, K.F. Chien, R.C. Kuo, Journal of Nuclear Materials 362 (2007) 93.
[15] R.S. Daum, S. Majumdar, Y. Liu, M.C. Billone, Journal of Nuclear Science and Technology 43 (9) (2006) 1054.
[16] C. Ferry, C. Poinssot, C. Cappelaere, L. Desgranges, C. Jegou, F. Miserque, J.P. Pirion, D. Roudil, J.M. Gras, Journal of Nuclear Materials 352 (2006) 246.
[17] F. Nagase, T. Fuketa, Journal of Nuclear Science and Technology 41 (12) (2004) 1211.
[18] M. Veleva, S. Arsène, M.-C. Record, J.L. Bechade, J.B. Bai, Metallurgical and Materials Transactions A 34A (2003) 567.
[19] S. Arsène, J.B. Bai, P. Bompard, Metallurgical and Materials Transactions A 34A (2003) 579.
[20] S. Arsène, J.B. Bai, P. Bompard, Metallurgical and Materials Transactions A 34A (2003) 553.
[21] M. Grange, J. Besson, E. Andrieu, Metallurgical and Materials Transactions A 31A (2000) 679.
[22] H. Tsai, M.C. Billone, Journal of ASTM International 3 (1) (2006) 14.
[23] C. Poinssot, C. Ferry, J.-M. Gras, Materials Research Society Symposium Proceedings 807 (2004) 29–34.
[24] Delayed hydride cracking in zirconium alloys in pressure tube nuclear reactors, Final report of a co-ordinated research project 1998–2002, 2004 IAEA-TECDOC-1410.
[25] S.-K. Kim, Journal of Nuclear Materials 378 (2008) 30.
[26] M. Sugisaki, K. Hashizume, Y. Hatano, Estimation of hydrogen redistribution in zircaloy cladding of spent fuel under thermal conditions of dry storage and evaluation of its influence on mechanical properties, IAEA-TECDOC-1316, International Atomic Energy Agency.
[27] M.P. Puls, Metallurgical Transactions A 19A (1988) 1507.
[28] M.P. Puls, Metallurgical Transactions A 22A (1991) 2327.
[29] M. Kerr, M.R. Daymond, R.A. Holt, J.D. Almer, Journal of Nuclear Materials 380 (2008) 70.
[30] S.I. Hong, K.W. Lee, Journal of Nuclear Materials 340 (2005) 203.
[31] H. Haysashi, K. Ogata, T. Baba, K. Kamimura, Journal of Nuclear Science and Technology 43 (9) (2006) 1128.
[32] H.M. Chung, Understanding hydride and hydrogen-related processes in high burn-up cladding in spent nuclear fuel storage and accident situations, in: Proceeding of the 2004 International Meeting on LWR Fuel Performance, Orlando, FL, September 2004 (Paper 1065).
[33] K.S. Chan, Journal of Nuclear Materials 227 (1996) 220.
[34] K.W. Lee, S.I. Hong, Journal of Alloys and Compounds 346 (2002) 302.
[35] J. Xu, S.-Q. Shi, Journal of Nuclear Materials 327 (2004) 165.
[36] M. Kuroda, S. Yamanaka, Journal of Nuclear Science and Technology 39 (3) (2002) 234.
[37] G. Bertolino, G. Meyer, J. Perez Ipina, Journal of Alloys and Compounds 330–332 (2002) 408.
[38] G. Bertolino, G. Meyer, J. Perez Ipina, Journal of Nuclear Materials 320 (2002) 272.
[39] G. Bertolino, G. Meyer, J. Perez Ipina, Journal of Nuclear Materials 322 (2002) 57.
[40] J. Bertsch, W. Hoffelner, Journal of Nuclear Materials 352 (2006) 116.
[41] K.S. Chan, Acta Metallurgica et Materialia 43 (1995) 4325.
[42] M.Y. He, A. Bartlett, A.G. Evans, J.W. Hutchinson, Journal of the American Ceramic Society 74 (1991) 767.
[43] R. Choubey, M.P. Puls, Metallurgical and Materials Transactions A 25A (1994) 993.
[44] K.-F. Nilsson, V. Vokál, Materials Science and Engineering A 502 (2009) 54.